Effect of composition and work hardening on solid solution decomposition in twin-roll cast Al-Mn sheets

M. Cieslar[1]* , M. Slámová[2], J. Uhlíř[2], Ch. Coupeau[3], J. Bonneville[3]

[1] *Charles University, Faculty of Mathematics and Physics, Ke Karlovu 5, CZ-121 16 Prague 2, Czech Republic*
[2] *Research Institute for Metals, Panenské Břežany, Ltd., Panenské Břežany 50, 250 70 Odolena Voda, Czech Republic*
[3] *LMP UMR6630 CNRS, Univ. de Poitiers, BP 30179, F-86962, Futuroscope – Chasseneuil Cedex, France*

Received 25 July 2006, received in revised form 1 March 2007, accepted 2 March 2007

Abstract

Fins in automotive heat exchangers are often manufactured from Al-Mn foils. The foils are usually prepared from ingot cast plates. The use of continuous twin-roll casting (TRC) instead of ingot casting substantially reduces energy and work consumption thus resulting in lower foil costs. The paper reports results of a study aimed at understanding the precipitation processes occurring during the annealing of two TRC Al-Mn based alloys differing in manganese and silicon content. The effect of work hardening level introduced by cold rolling prior to annealing was evaluated. Precipitation was studied by resistometric measurements in the course of a stepwise heating from room temperature to 500 °C. Transmission electron microscopy examinations of specimens quenched from temperatures of expressive changes in resistivity helped to identify the microstructural processes responsible for resistivity changes. The corresponding reflections in mechanical properties were monitored by hardness measurements.

K e y w o r d s: Al-Mn alloys, twin-roll casting, phase transformations, recrystallization

1. Introduction

Thin foils manufactured from aluminium alloys are used as fins in automotive heat exchangers. Aluminium tubes and fins in exchangers are joined together by brazing at temperatures very close to the melting point of the joined alloys. Recrystallization and significant grain coarsening can occur in the fins during brazing resulting in deterioration of fin strength and by this, in exchangers sagging. Grain coarsening can be prevented in alloys of suitable composition by appropriate thermo-mechanical processing. Precipitates of suitable size and separation formed during processing can pin grain boundaries and thus hinder grain coarsening [1]. Therefore, the alloy composition and processing parameters must be carefully adjusted in order to obtain materials of required microstructure and properties.

The usual thickness of heat exchanger foils is of 70 μm. Foils are manufactured by hot and cold rolling from ingot cast plates of thickness larger than 200 mm. However, they can also be produced by cold rolling of continuously twin-roll cast (TRC) strips of thickness smaller than 10 mm. Therefore, continuous casting leads to substantial shortening of the technology, resulting in energy and work consumption savings and finally in lower foil cost [2, 3]. It must be pointed out that TRC casting produces alloys with considerably higher solid solution saturation as compared to ingot cast alloys. For this reason, the processing of TRC materials is rather different from that used for ingot cast alloys. The development of the appropriate processing route needs a thorough knowledge of the physical-metallurgical processes occurring during manufacturing.

The decomposition of the supersaturated solid solution in two TRC Al-Mn alloys and the transformation of primary phases occurring during annealing were studied. The paper reports the results of this study that were focussed on the effect of manganese and silicon content on the temperature and intensity of transformations. The effect of work hardening induced by cold rolling prior to annealing was also evaluated.

*Corresponding author: tel.: +420 2 2191 1356; fax: +420 2 2191 1490; e-mail address: Miroslav.Cieslar@mff.cuni.cz

Table 1. Composition of experimental materials (in wt.%)

Alloy	Mn	Si	Fe	Cu	Mg	Zn	Ti
A	1.13	0.11	0.32	0.14	0.003	0.013	0.044
B	1.00	0.62	0.32	0.15	0.003	0.067	0.044

2. Experimental

AL INVEST Břidličná, a.s. provided two TRC Al-Mn alloys, whose composition is in Table 1. The alloy with low silicon and high manganese contents is further referred to as A, the alloy with high Si content and low Mn as B, respectively. Both alloys were twin-roll cast in strips of 8.5 mm in thickness and cold rolled to thickness of 1.4 mm (A1 and B1) and 0.4 mm (A04 and B04), respectively. Specimens with true strain ε equal to 2.1 and 3.5, respectively, were thus produced and then subjected to an isochronal annealing. The annealing was carried out using a step-by-step heating program with steps 20 ℃/20 min in the temperature range from room temperature (RT) up to 500 ℃. Solid solution decomposition was investigated by measurements of specimen electrical resistivity ρ in liquid nitrogen (−196 ℃). The DC four-point measuring method with a dummy specimen in series was used.

The residual resistivity ratio (referred to as RRR) was determined for specimens quenched from several temperatures corresponding to expressive changes in resistivity. RRR is the ratio of resistivities at RT and −196 ℃, respectively, and since it is a ratio of values measured on the same specimen, it does not depend on specimen shape, thickness, etc. Therefore, the determination of RRR enables the direct comparisons of specimens of different size and shape. It is worth mentioning that in diluted aluminium alloys the evolution of RRR is similar to that observed for electrical conductivity κ. The contribution of solute atoms to κ (and also to $\rho = 1/\kappa$) and RRR is much higher than that of intrinsic crystal defects [4, 5]. The absolute value of RRR provides information about the amount of solute atoms dissolved in the matrix. Therefore, higher RRR value corresponds to higher purity of the matrix, i.e., to larger amount of solutes bound in precipitates and primary phases.

The recrystallization response curves of the materials were obtained by measurements of Vickers hardness HV 1. In addition, nanoindentation measurements were carried out on foils of 70 μm thickness prepared from alloy A. Nanoindentation measurements allowed to determine Young's modulus, which is an important characteristic of the material in industrial applications. Prior to nanoindentation, 45 foil pieces were stacked together, mounted in a holder and then mechanically polished on their long transverse plane (parallel with the rolling direction). Nanoindentations were performed at RT using a Nano-Hardness Tester CSEM Instruments, equipped with a Berkovitch tip and working in the force-controlled mode. The time schedule of the nanoindentation tests was as follows: 30 s loading, 30 s sustaining the load, 30 s unloading. Loads ranging from 1 to 30 mN were applied. The indents were positioned on a line parallel with foil normal and were sufficiently spaced to prevent the occurrence of interactions between them and with foil interfaces. The reduced Young's modulus E^* (Eq. 1) and hardness value were deduced from (load-indent depth) curves using the method reported in [6]:

$$E^* = \frac{E}{(1-\nu^2)}, \tag{1}$$

where E is the Young's modulus and ν is the Poisson's ratio of the material.

The substructure of deformed and annealed specimens, the particles of primary phases and the precipitates formed during annealing were studied by transmission electron microscopy (TEM). Observations were carried out at 200 kV using a JEOL JEM 2000 FX microscope equipped with an X-ray energy dispersive spectrometer (EDX) LINK AN 10 000. TEM foils were prepared parallel to sheet rolling plane. Observations were performed only on A04 and B04 specimens in conditions corresponding to significant points of resistivity annealing spectra.

3. Results

3.1. Electrical resistivity measurements

Figure 1 shows the electrical resistivity annealing curves $(\rho - \rho_0)/\rho_0 = f(T)$ of all specimens; ρ_0 designates the resistivity at the beginning of annealing. The most important feature of the curves is the pronounced resistivity drop between 260 ℃ and 440 ℃. The drop is preceded by moderate changes at temperatures below 260 ℃. Furthermore, all alloys exhibit a resistivity increase of small magnitude above 460 ℃. The annealing curves can thus be divided into several parts with different rates of resistivity change. The negative differential curves $-(\mathrm{d}\rho/\mathrm{d}T)/\rho_0$, referred to as resistivity annealing spectra, were calculated and plotted in Fig. 2. The resistivity spectra exhibit several peaks, corresponding to the resistivity changes shown in Fig. 1. High peaks of complicated shape are observed above 260 ℃ giving the evidence of complex processes occurring in the material within the temperature interval from 260 ℃ to 440 ℃.

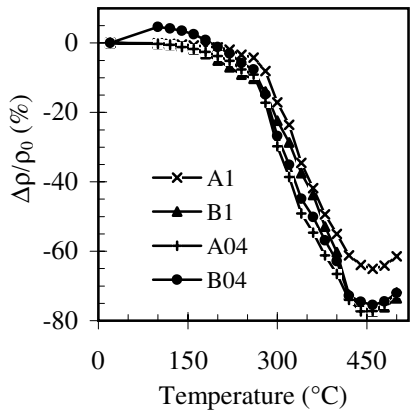

Fig. 1. Evolution of electrical resistivity as a function of temperature during the step-by-step heating. ρ_0 is the resistivity at the beginning of annealing, $\Delta\rho$ is the difference between the resistivity ρ at temperature T and ρ_0.

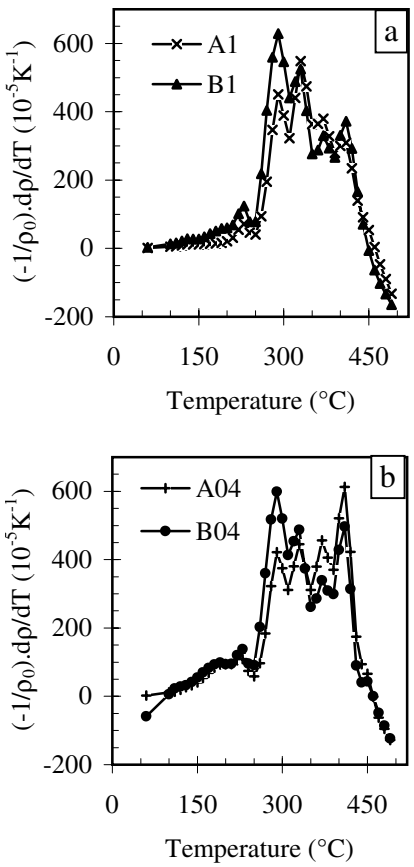

Fig. 2. Resistivity annealing spectra calculated from resistivity data: $-(\mathrm{d}\rho/\mathrm{d}T)/\rho_0$ as a function of temperature: a) specimens A1 and B1 with thickness of 1.4 mm; b) specimens A04 and B04 with thickness of 0.4 mm.

The evolutions of resistivity with temperature in A and B specimens differ only slightly. Also, the influence of strain ε is not big. Nevertheless, the curves

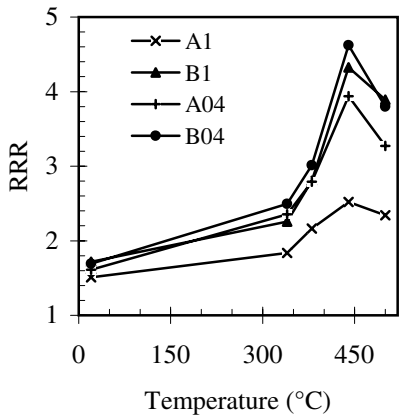

Fig. 3. Changes of the residual resistivity ratio (RRR) as a function of annealing temperature.

exhibit several interesting features. Below 260 ℃, the resistivity of both alloys decreases only moderately. The decrease is slightly more intensive in the specimens with larger ε (A04, B04). Resistivity evolution does not depend on ε in the temperature range from 260 ℃ to 360 ℃, in contrast to temperatures below 260 ℃. On the other hand, between 260 ℃ and 360 ℃, the curves form two groups: the peaks of specimens B with high Si content are higher than these of specimens A. Surprising evolution is observed above 360 ℃. The shape of the peaks between 360 ℃ and 450 ℃ does not depend on composition. In this temperature range, the effect of strain dominates. Above 450 ℃ up to 500 ℃, the resistivity spectra exhibit negative values that reflect an increase in resistivity (Fig. 1).

Figure 3 shows how RRR values change with increasing temperature during the step-by-step annealing. Since the initial cold rolled state, RRR values differ, the same as after annealing. At each temperature, they are (except for 340 ℃) lower in A specimens, i.e., the influence of composition dominates. At low annealing temperatures (up to 340 ℃), RRR slowly rises in all materials. A fast increase occurs above 340 ℃ with a maximum at 440 ℃. Above 440 ℃, up to 500 ℃, the pronounced drop in RRR is observed.

3.2. Hardness

Plots of Vickers hardness HV 1 as a function of annealing temperature are shown in Fig. 4. The initial hardness is higher in the specimens with higher ε. The specimen B1 with higher silicon content exhibits higher HV 1 value. No difference in hardness is observed in specimens A04 and B04 with higher strain $\varepsilon = 3.5$, neither in the initial state nor after annealing to 200 ℃. The annealing below 200 ℃ results in almost negligible decrease in hardness that does not depend on composition. Above 200 ℃, HV 1 drops in two stages. The positions of the stages on the tem-

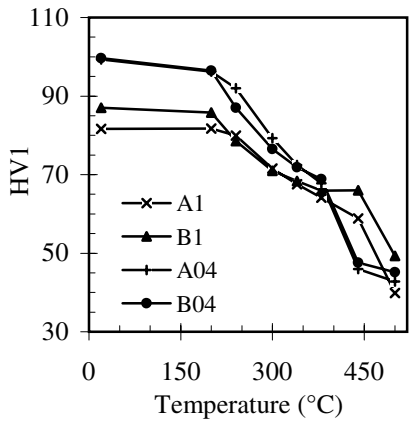

Fig. 4. Changes of Vickers hardness HV 1 as a function of annealing temperature.

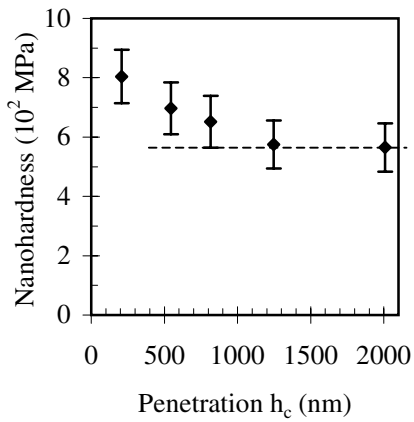

Fig. 5. Evolution of nano-hardness as a function of penetration depth.

perature scale are evidently influenced by ε. In the specimens A04 and B04, the borders between the two stages are at 380 ℃, while in the specimens with low ε (A1 and B1) the end of the first stage is shifted by 60 ℃ to higher temperatures.

Figure 5 shows the evolution of nano-hardness as a function of penetration depth. Each data point is an average of more than eight values. The error bars correspond to the mean standard deviations. A constant hardness value of (0.57 ± 0.1) GPa is achieved at penetration depths beyond 1 μm. Furthermore, E^* does not depend on penetration depth and exhibits a constant value of (86 ± 4) GPa.

3.3. Microstructure

Before annealing, heavily deformed structure is observed by TEM in both alloys (Fig. 6a). No dynamic recrystallization is evident in any of the specimens even in the specimens with high ε. Colonies of primary phases particles (formed at solidification) rich in Al, Fe, Mn in both alloys and also in Si in alloy B, are observed on dendrite cell boundaries (Fig. 6a). Indi-

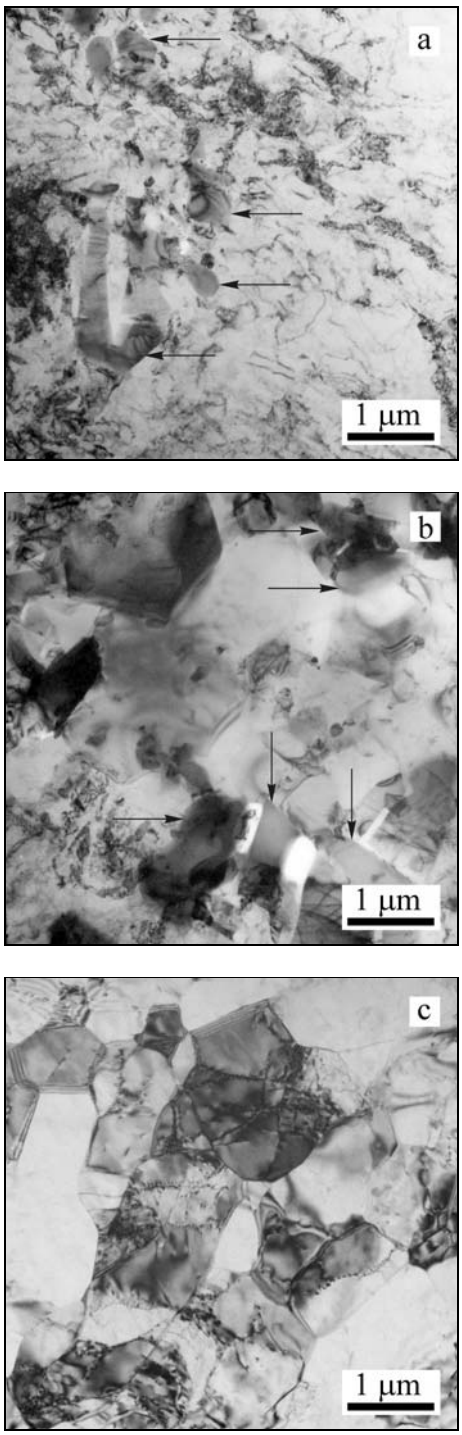

Fig. 6. TEM images showing the evolution in specimen A04: a) heavily deformed matrix on the as-rolled specimen, arrows indicate an eutectic colony of primary particles (initial); b) recrystallization nuclei at primary particles (the particles are indicated by arrows) in the specimen annealed up to 240 ℃; c) largely recovered substructure of the specimen annealed to 340 ℃.

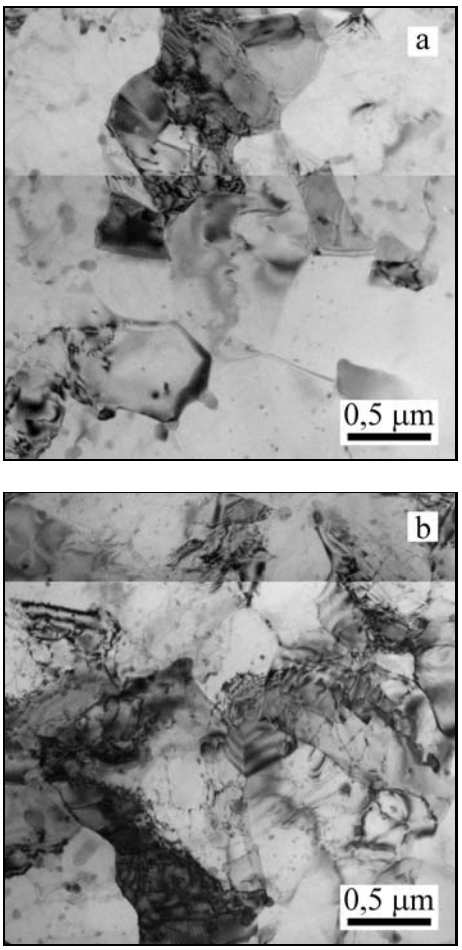

Fig. 7. TEM images of the recovered substructure in specimens A04 (a) and B04 (b) annealed up to 380 °C. Dispersion of tiny Mn-rich precipitates is observed in specimen B04 and at smaller extent in A04.

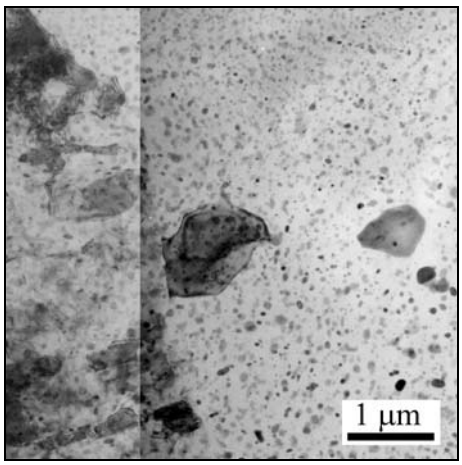

Fig. 8. TEM image of specimen A04 annealed up to 440 °C showing a dense population of precipitates and a recrystallization front.

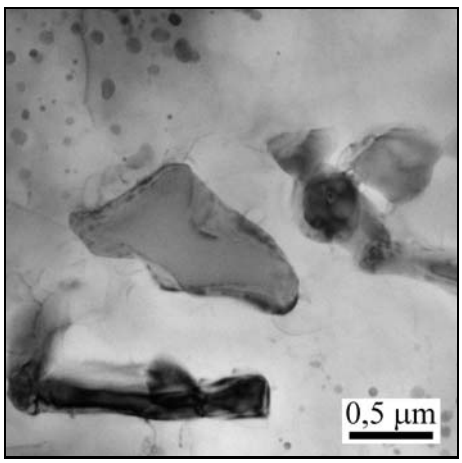

Fig. 9. TEM image of specimen B04 annealed up to 500 °C showing a precipitate-free zone in the vicinity of a former eutectic colony.

vidual particles of Si are observed in the interdendrite spaces in alloy B with high Si content but they are not present in alloy A (low Si content).

TEM observations of specimens annealed up to 240 °C reveal no significant changes in dislocation substructure as compared to the as-rolled condition. In the vicinity of eutectic colonies, small recrystallization nuclei are observed in specimen A04 (Fig. 6b) but not in specimen B04.

Annealing up to 340 °C causes partial recovery of deformation substructure and a large fraction of specimen volume consists of well-defined subgrains (Fig. 6c). Simultaneously, nuclei growth occurs in the vicinity of primary particles in specimen A04, whereas only first nuclei formation is observed in specimen B04. At this temperature, very small dispersoids are occasionally observed in the interdendrite spaces of B04 specimen but not in A04. These particles are rich in Mn, the presence of Si and Fe was not detected. Since the characteristic X-ray radiation of Si is strongly absorbed by Fe and Mn atoms in the constituents and the size of particles is small, the presence of Si in the dispersoids cannot be completely denied or proved by EDX.

At 380 °C, the substructure is fully recovered and polygonized in 70 % of specimen volume. Only 30 % of the volume is recrystallized with grains of 1–2 μm in diameter. Furthermore, locally in both specimens, the precipitation of ellipsoidal or spherical dispersoids occurs (Fig. 7). These particles are of the same nature as the ones observed at 340 °C in B04 specimen but they are coarser (10–100 nm). Their massive formation is observed everywhere in both specimens annealed up to 440 °C (Fig. 8). The precipitation is accompanied by recrystallization and grain growth. Precipitation-free zones (PFZ – Fig. 9) are observed in the vicinity of former eutectic colonies. Nearly 95 % of speci-

men volume is recrystallized at 440 °C. Complete recrystallization, further coarsening of precipitates and formation of precipitation-free zones were observed in specimens annealed up to 500 °C.

4. Discussion

In both alloys, the initial states contain colonies of particles of primary phases rich in Al, Fe, Mn and Si. They are formed by eutectic reaction at solidification. In an alloy with low silicon content (A04), they are representatives mainly of the non-equilibrium Al_6(Fe,Mn) phase and at less extent of the α-Al(Mn,Fe)Si phase referred to as $Al_{12-15}(Mn,Fe)_3Si_{1-2}$ [7, 8]. It is worth mentioning that the latter contains a larger amount of manganese. In the Si-rich alloy (B04) only the silicon containing α-phase forms at casting. The composition and crystallographic nature of Al-Mn-Fe-Si phases in Al-Mn based commercial alloys [7–9] are well known for ingot cast materials. However, in TRC alloys the primary particles are formed at much more non-equilibrium solidification conditions. Thus, they can significantly differ from the phases in ingot cast materials. Furthermore, due to TRC high solidification rate, the particles are small and their direct analysis, i.e. by TEM, is more difficult as compared to ingot cast alloys.

RRR allows the estimation of solutes concentration in the supersaturated solid solution. Therefore, the observed changes in resistivity and RRR are mainly caused by the redistribution of solutes while the role of intrinsic defects is only indirect. Moreover, it is well known [10, 11] that the Mn dissolved in the matrix affects resistivity (and RRR) much more strongly than Fe and Si. Due to the very low solubility of Fe in Al, the direct impact of Fe on RRR values can be ignored. The RRR values of the investigated specimens differ since their initial state and the influence of composition dominates. At each temperature, including the highest temperature (500 °C), they are (except for 340 °C) lower in A specimens. This result indicates that the solute content of Mn in the matrix is higher in the alloy containing more Mn.

In the temperature range below 240 °C, only a small decrease in resistivity and a small increase in RRR were observed. The extent of changes is larger in the specimens with bigger ε and also slightly higher in B specimens. High dislocation density was observed in the specimens annealed up to 240 °C and is supposed to enhance the pipe diffusion of solutes, namely that of Si. It is worth mentioning that Si diffusion velocity at all temperatures is much higher than that of Mn and Fe. Si atoms therefore can move on long distances to the colonies of primary phases causing their enrichment. Since the number of coarse compounds is only limited and the annealing temperature is too low, the massive long-distance bulk diffusion does not occur. Therefore, the depletion of the matrix from Si itself does not affect significantly resistivity and RRR, as was also observed in our experiments. However, the depletion of the matrix from Si in the vicinity of colonies results in lower pinning of the moving dislocations in these regions. For this reason, the recovery process and the formation of first recrystallization nuclei begin preferably in areas close to eutectic colonies. Moreover, this process may be enhanced by the presence of zones with high dislocation density formed in the vicinity of the colonies of coarse particles [1] due to the localization of deformation. Below 240 °C, the volume fraction of areas recovered is low and their impact on mechanical properties is weak (see Fig. 4). An additional process may be expected at low temperatures. Pipe diffusion of Si on short distances can result in clustering of this solute and would be manifested by resistivity changes. Such clustering is easier in interdendrite spaces where the number of primary particles is small.

The increase in RRR above 240 °C indicates that further depletion of the matrix from solutes occurs, enhanced by bulk diffusion of Si to eutectic colonies and by short-range diffusion of Mn in the vicinity of colonies.

At low temperatures, the diffusivity of Mn atoms is low [8] and they can move only on short distances. Therefore, at low temperatures Mn is supposed to participate in two simultaneous processes [12]:

1. In interdendrite spaces, decomposition of the supersaturated solid solution can occur by precipitation of Mn in Al_6Mn or Al_6(Mn,Fe) phases, and together with Si, in α-Al(Mn,Fe)Si dispersoids. The precipitation of α-Al(Mn,Fe)Si dispersoids may be facilitated by the clustering of Si atoms at low temperatures.

2. In the vicinity of eutectic colonies, Mn and Si can move to primary Al_6(Mn,Fe) particles taking part in their transformation into α-Al(Mn,Fe)Si phases. The enrichment in Mn and Si of the primary phases rises the width of the Mn and Si depleted zones [8, 9]. This increase may provoke the dissolution of the unstable α-Al(Mn,Fe)Si dispersoids in these zones and may result in the formation of PFZ (as observed experimentally also by the present authors). The Si and Mn atoms from these previous dispersoids easily diffuse to the primary particles and participate in their transformation into α-Al(Mn,Fe)Si phase.

The transformation at 280 °C is evidently more intensive in the Si-rich alloy confirming the crucial role of Si long-range diffusion to primary particles at these temperatures. Similar behaviour is typical for Si containing cold-rolled Al alloys in the temperature range 240–340 °C [10]. Due to the partial recovery of dislocation substructure, facilitated also by depletion of the matrix from Si atoms, a significant drop in hardness is observed above 240 °C.

High peaks in resistivity spectra and a pronounced increase in RRR values are observed at temperatures above 340 °C. They are more intensive in Mn-rich alloy. Moreover, their shape depends on true strain ε. In the specimens deformed to higher ε, generally higher peaks are observed. As discussed above, the Si atoms from solute solution are expected to be bound in the transformed primary particles either directly by bulk diffusion at relatively low temperatures or through dissolution of α-Al(Mn,Fe)Si dispersoids in their vicinity at higher temperatures. The Al_6(Mn,Fe) phase is known [13] to precipitate predominantly on dislocation cell walls and subgrain boundaries. Therefore, the split peaks observed between 340 °C and 440 °C can be attributed again to two simultaneous processes revealed by TEM examinations: a) formation of Al_6(Mn,Fe) dispersoids on subgrain boundaries; b) enrichment in Mn and Si of the primary particles, their transformation in α-Al(Mn,Fe)Si and their coarsening. The peak is higher in the alloy with higher Mn content that suggests that the long-range diffusion of Mn, accompanied by transformation of Al_6(Mn,Fe) into α--Al(Mn,Fe)Si phase (richer in Mn), dominates in this temperature range.

The final decrease of RRR and moderate increase in resistivity above 460 °C is caused by a partial particle dissolution resulting in the re-enrichment of the solid solution in Mn and Si.

The initial hardness is higher in the specimens with higher ε that indicates a larger amount of stored deformation energy. At temperatures up to 380 °C, recovery is the dominant softening process. The significant drop in hardness above this temperature is caused by recrystallization. A shift by 60 °C to higher temperatures of the start of the abrupt drop in HV is observed in the material with lower ε independently on alloy composition. This shift is due to the lower stored deformation energy known to be the main driving force of recrystallization [13]. Therefore, the shift of recrystallization towards higher temperatures could not be ascribed to pinning of subgrain and grain boundaries by precipitates. On the other hand, TEM observations indicate that the formation of recrystallization nuclei in the vicinity of eutectic colonies is postponed in the alloy with high Si content. This effect is probably due to the more intensive effect of solute atoms (namely Si) on the dislocation mobility during recovery.

In the specimens with high Mn and low Si content (alloy A), the values of RRR are lower as compared to alloy B. This difference is observed not only at temperatures of massive precipitation but also at high temperatures when back dissolution of small dispersoids and solution enrichment, especially in Mn, occurs. Therefore, significantly higher residual concentration of dissolved Mn is expected at the end of annealing in alloy A, especially in specimen A1. It can be assumed that the observed difference is due to the fact that in the alloy with lower Si content less Mn atoms are bound both in precipitates and transformed primary compounds. High residual Mn solute content is of big importance in industrial applications, especially in heat exchangers, because it is connected with low electrical and thermal conductivity, which could be an important drawback in heat exchangers.

The Young's modulus determined by nanoindentation measurements in foils of 70 μm thickness is of 76 GPa, which is slightly higher than value usual for bulk material (70 GPa) [7]. This result indicates that the highly deformed surface layers of the foil have substantial impact on its mechanical properties. The effect of the modulus of the oxide layer, higher than that of Al, can be also important in the case of thin foils because its thickness could not be neglected.

5. Conclusions

This study was performed in order to determine the influence of alloy composition and strain on recovery and recrystallization processes in twin-roll cast Al-Mn based alloys. The electrical resistivity measurements during model isochronal annealing indicated that the difference between evolutions of resistivity in specimens with different composition is relatively small. Nevertheless, the shape of the annealing and RRR curves evidences that the composition and strain prior to annealing influence the process of solid solution decomposition. The results of the study allow selecting the temperature range of industrial annealing, which ensures the formation of a dispersion of suitably sized precipitates able to effectively pin grain boundaries in the material during foil brazing.

Acknowledgements

The financial support of the Ministry of Education, Youth and Sports of the Czech Republic provided in the framework of project No. 1M2560471601 is gratefully acknowledged. Two of the authors (C. Coupeau and J. Bonneville) would like to acknowledge the financial support provided by BARRANDE project 2004-039-2.

References

[1] HUMPHREYS, P. J.—HATHERLY, M.: Recrystallization and Related Annealing Phenomena. Oxford, Pergamon 1995.
[2] LI, B. Q.: JOM, *47*, 1995, p. 13.
[3] JAMET, M.: Aluminium Today, *11*, 1999, p. 19.
[4] BROWN, R. A.: J. Phys. F: Metal. Phys., *7*, 1977, p. L297.
[5] HARRISON, W. A.: Pseudopotentials in the Theory of Metals. New York, W. A. Benjamin, Inc. 1996.

[6] OLIVER, W. C.—PHARR, G. M.: J. Mat. Res., *7*, 1992, p. 1564.
[7] HATCH, J. E.: Aluminum. Properties and Physical Metallurgy. 1st edition. Metals Park, Ohio, ASM 1984.
[8] ALEXANDRE, D. T. L.—GREER, A. L.: Acta Mater., *50*, 2002, p. 1.
[9] DEHMAS, M. et al.: Aluminium, *80*, 2004, p. 619.
[10] SLÁMOVÁ, M.—KARLÍK, M.—CIESLAR, M.—CHALUPA, B.—MERLE, P.: Kovove Mater., *40*, 2002, p. 389.
[11] SLÁMOVÁ, M.—KARLÍK, M.—CIESLAR, M.—CHALUPA, B.—MERLE, P.: Kovove Mater., *41*, 2003, p. 51.
[12] LI, Y.—ARNBERG, L.: Materials Science Forum, *396–402*, 2002, p. 875.
[13] CHEN, S. P.—KUIJPERS, N. C. W.—VAN DER ZWAAG, S.: Mater. Sci. Eng., *A341*, 2003, p. 296.